



Effects of AlSi12 interlayer on microstructure and mechanical properties of laser welded 5A06/Ti6Al4V joints

Xiongfeng Zhou¹ · Xiaobing Cao¹ · Fan Zhang² · Zhi Chen³ · Ji'an Duan¹

Received: 6 August 2020 / Accepted: 8 April 2021 / Published online: 22 April 2021
© International Institute of Welding 2021

Abstract

The morphology of the weld seam, the formation mechanism of interface, and the microstructure and mechanical properties of both direct and AlSi12 (ER4047)-added dissimilar 5A06Al/Ti6Al4V lap joints were investigated, respectively. The Gibbs free energies of intermetallic compounds, such as TiAl₃, TiAl, and Ti₃Al, were calculated. The results showed that the interface layers were mainly composed of Ti₃Al, TiAl, and TiAl₃, and the order of them was TiAl₃, TiAl, and Ti₃Al from outside to inside. The addition of ER4047 interlayer could suppress the formation of IMCs and reduce the micro-cracks in TiAl₃ layer. The ER4047-added joints featured good mechanical properties, i.e., the shear strength of 2087 N, 2405 N, and 2157 N respectively, which were much higher than the shear strength of 1721 N for the direct joint. Furthermore, the fracture model of the direct joint was brittle fracture, while that of the ER4047-added joints was quasi-cleavage. The results can provide theoretical guidance for the prediction of Ti/Al interface reaction and welding of other dissimilar metals.

Keywords Laser penetration welding · ER4047 interlayer · Gibbs free energy · Shear strength · Micro-hardness · Fracture

1 Introduction

In aeronautical and automotive industries, the combination of light weight and excellent mechanical properties has been a critical factor in material selection [1]. Given the high specific strength, superior toughness, and corrosion resistance and low density, titanium alloys have exhibited great application prospect in aerospace and vehicle industries, while aluminum alloys are widely used in these fields due to the characteristics of low weight, better weldability, and low cost [2, 3]. In recent years, multi-material structures have shown a higher demand

for performance [4], and the Ti/Al hybrid structures have attracted great attention and become relevant for application in aerospace, shipbuilding, and automotive industries because of the integration of excellent performances for titanium alloy and aluminum alloy [5, 6]. For example, the wing skin and engine of the plane, the pipeline of the satellite propulsion system, the safety track of aviation seat, and the automobile exhaust system have been reported to use the Ti/Al hybrid structures for further weight reduction and functional diversification [7, 8].

The wide application of Ti/Al hybrid structures puts forward higher requirements for welding technology and process. However, the welding process of titanium to aluminum is full of challenges due to the great differences of physical and chemical properties of them [9, 10]. Specifically, the lattice size and thermal expansion coefficient of titanium and aluminum are very large, which makes it difficult to produce a metallurgical reaction and easy to crack. Moreover, the brittle intermetallic compounds (IMCs), such as TiAl₃, TiAl, and Ti₃Al, which deteriorate the properties of joints, are easily formed during the welding process [11, 12]. Therefore, controlling the metallurgical reaction of the interface and improving the composition of IMCs are beneficial to obtain high performance Ti/Al welded joints.

In order to reduce the joint brittleness, many researches have used interlayer to adjust the weld composition and

Recommended for publication by Commission X - Structural Performances of Welded Joints - Fracture Avoidance

✉ Fan Zhang
zhangfan219@csu.edu.cn

✉ Ji'an Duan
duanjian@esu.edu.cn

¹ State Key Laboratory of High Performance and Complex Manufacturing, College of Mechanical and Electrical Engineering, Central South University, Changsha 410083, China

² School of Automation, Central South University, Changsha 410083, China

³ College of Vehicle Engineering, Hunan Biological and Electromechanical Polytechnic, Changsha 410127, China

change the composition of IMCs [13]. Amlan Kar et al. [14] studied the influence of niobium interlayer in friction stir welding of pure aluminum to grade 2 titanium. The research results showed that both the Ti particles and Nb particles were homogeneously distributed and Nb restricted the reaction between Ti and Al as well as the formation of brittle Al_3Ti intermetallic phase. A.N.Alhazaa et al. [15] reported that the Cu coatings could not only inhibit oxide layer at the Al7075 alloy surface but also improve the wettability on both alloy surfaces during the diffusion bonding of Al7075 to Ti6Al4V using Cu coatings and Sn-3.6Ag-1Cu as interlayer. Samavatian M et al. [16] realized the reliable connection between Al2024 and Ti6Al4V alloy with transient liquid phase welding by using Cu-Zn interlayer. Their results suggested that the addition of Cu-Zn interlayer could reduce the brittle IMCs such as $TiAl_3$ at the interface, while various other IMCs like Al_2Cu , $TiCu_3$, Ti_2Cu , $TiZn_{16}$, and $Al_{4.2}Cu_{3.2}Zn_{0.7}$ were formed at the interface. Haodong Wang et al. [17] investigated the TIG welding-brazing of Ti6Al4V and Al5052 in overlap configuration by using zinc foil as the interlayer. It was found that the adding of zinc foil interlayer could significantly improve the wettability and spreading ability of the Al-Si filler on the Ti6Al4V sheet. Although the welding processes mentioned above have been reported to realize the connection of the titanium and aluminum, these processes are generally more complex and less controllable [18, 19]. Researchers have gradually begun to use laser welding technology to weld Ti/Al lap joints, and the research about the effect of aluminum-based interlayer on the properties of Ti/Al dissimilar lap joints is relatively limited. In addition, the thickness of the interlayer, an important determinant of the thickness and morphology of the reaction layer, is rarely discussed in detail.

The present research is to investigate the effect of thickness of ER4047 interlayers on macroscopic and microscopic structural evolution and mechanical properties. Mostly, the characteristics of the laser penetration welding of Ti6Al4V titanium to 5A06 aluminum without and with ER4047 (AlSi12) interlayer under the lap configuration were investigated in detail. The macroscopic surface, cross section properties, and the microstructure at the weld seam/Al interface of both direct joints and ER4047-added joints were analyzed. The phase and the formation order of intermetallic compounds (IMCs) at the weld seam/Al interface were emphatically explored. Moreover, the shear properties and the fracture mechanism of both direct and ER4047-added joints were discussed.

2 Experimental details

2.1 Materials preparation

The Ti6Al4V titanium plate with specification of $50\text{ mm} \times 60\text{ mm} \times 1.5\text{ mm}$ and 5A06 aluminum alloy plate with

specification of $50\text{ mm} \times 60\text{ mm} \times 2.0\text{ mm}$ were prepared in this work, respectively. In addition, the ER4047 foil with different thickness of 0.1 mm, 0.2 mm, and 0.3 mm was used as interlayer. The 5A06 alloy with high corrosion resistance and excellent welding performance is a non-heat treatment strengthened aluminum alloy [20]. The annealed Ti6Al4V alloy used at this experiment is $\alpha+\beta$ titanium alloy containing about 9–30% β phase [21, 22]. The ER4047 is an aluminum-based brazing alloy with low melting point and excellent wettability. The elementary compositions and physical and mechanical properties of the materials at room temperature are illustrated in Tables 1 and 2, respectively.

Before the welding experiment, it is necessary to eliminate surface contamination of the samples. The 5A06 plates were soaked in acetone, 20% (in mass) NaOH, and 30% (in mass) HNO_3 , respectively, for a few minutes to remove oil and oxide layer. The Ti6Al4V plates were also immersed in acetone and the weak acid solution (5 mL HF, 30 mL HNO_3 , 65 mL H_2O), respectively, for several minutes to remove oil and oxides. Moreover, both the parent plates and the ER4047 foil were dried at $50\text{ }^\circ\text{C}$ for 10 min.

2.2 Laser welding procedures

Laser penetration welding was conducted on a self-built optical fiber laser welding platform with the maximum power of 1.2 kW, in which the laser beam with Gaussian distribution was delivered by a welding head equipped with collimating lens with 100 mm focal length and focusing lens with 200 mm focal length. The wavelength of the fiber laser is 1070 nm, and the size of the final focal spot is about 0.2 mm. A lap joint configuration of Ti6Al4V plate on 5A06 plate was performed with an overlapping distance of 20 mm. The laser beam was adjusted at an acute angle to the horizontal plane (85°) to prevent the lens group in welding head from being damaged by the reflected laser. According to previous experiments [23], the upper and lower parts of the plate were protected by high purity argon, and the flow rates were 20 L/min and 10 L/min, respectively. The welding configuration is shown in Fig. 1, and the specific parameters are listed in Table 3.

2.3 Mechanical properties test

After welding, the shear testing was executed to assess the strength of the joints with different thickness of ER4047 interlayer. Three identical samples were tested in order to reduce the error of experimental results, and the samples were cut by linear cutting machine (Proline EDM, DK773). Figure 2 exhibits the setup of the shear test, and the geometry size shown in Fig. 2b was designed with reference to GB/T 228-2002 criteria. The shear test was carried out at room temperature using tensile testing machine (SUST, CMT5150) under a stretching speed of 2 mm/min.

Table 1 Chemical composition of 5A06 and Ti6Al4V alloys

Alloy	Elements (wt.%)												
	Al	Ti	Mg	Si	Cu	Mn	Fe	Zn	V	C	N	H	O
5A06	Bal.	0.02	6.8	0.4	0.1	0.8	0.1	0.2	-	-	-	-	-
Ti6Al4V	6.2	Bal.	-	-	-	-	0.1	-	4.1	0.01	0.01	0.02	0.11
ER4047	Bal.	0.15	0.1	11.9	0.2	0.1	0.2	0.2	-	-	-	-	-

Unlike the shear samples, the cross section of the micro-hardness testing samples with the size of 10 mm × 6 mm was polished by water-sand paper of 180 # to 2000 # grit in turn after cutting, and the Vickers hardness tests of the welded joints were performed along the micro-hardness line under a load of 200 g and a holding time of 10s by using digital micro-hardness tester (Vegour, HVS-1000Z).

2.4 Weld characterization and phase determination

Transverse sections of the metallographic specimen were also first mechanically rough polished by water-sand paper of 180# to 7000# grit in turn and then precision polished by the aluminum oxide suspension with particle size of 0.5 μm. The macroscopic graph of weld seam surface and transverse section of the metallographic specimens were obtained by three dimensional optical microscope (Keyence, VHX-5000). The microstructure and element distribution of the weld cross section was investigated by scanning electron microscope (SEM, Tescan, MIRA 3 LMU) equipped with energy dispersive X-ray spectroscopy (EDS). The phase composition of the interface layer was recognized by the X-ray diffractometer (XRD, Japanese Electronics, Rigaku Rapid IIR).

3 Results

3.1 Weld seam morphology

3.1.1 Top surface appearance

Figure 3 shows the top surface appearance of the welded joints with various thicknesses of ER4047 interlayers. It can be noticed that the top surface of the direct joints shown in Fig. 3a is relatively rough, and only several masses of spatters are distributed at the beginning of welding. After adding ER4047

interlayer, dispersive spot spatters distribute around the weld seam, and the number of spatters increases with the ER4047 thickness, while the top surface of weld seam becomes more uniform than the direct joints, as shown in Fig. 3b–d. That can be explained that the addition of ER4047 interlayer aggravates the instability of laser keyhole and the bubbles originating from the low melting point alloying elements break more easily, resulting in the increase of fine and dense spatters [24–26]. Moreover, the recoil pressure of evaporation is the important factor causing welding spatters [27, 28]. It can be observed from the Fig. 3e that whether or not the ER4047 interlayer is added; regular wavy welds are produced under the action of upward melt flow, surface tension, and airflow circle; and the orientation of wave pattern is opposite to the welding direction (V), as shown in Fig. 3f.

3.1.2 Cross section appearance

Macroscopic cross section of the joints is shown in Fig. 4a. In addition to matrix, the typical cross section of the joint is divided into weld seam zone, titanium heat affected zones (HAZ 1), ER4047 heat affected zone (HAZ 2), and aluminum heat affected zone (HAZ 3). In order to better characterize the weld seam geometry, the weld width (W_w), weld depth (D), penetration depth of titanium into aluminum (P), and weld width at the upper coincidence surface (W_c) are defined, respectively. Moreover, the depth to width ratio (R_w) and penetration depth to width ratio (R_p) are also defined to characterize the whole weld seam and the penetration layer geometry. The weld depth to width ratio (R_w) and penetration depth to width ratio (R_p) are calculated by the equation $R_w = D/W_w$ and the equation $R_p = P/W_c$, respectively. It is not difficult to find that the value of P and W_c should be reduced as far as possible in terms of restraining the formation of IMCs, but in terms of ensuring the conductivity, thermal conductivity and shear strength of joints, P , and W_c should be kept to a certain value [2].

Table 2 Physical and mechanical properties of base materials: density (D), thermal conductivity (TC), coefficient of linear expansion (CLE), tensile strength (TS), yield strength (YS), and elasticity modulus (EM)

Alloy	D (g/cm ³)	TC (W/(m·K))	CLE (K ⁻¹)	TS (MPa)	YS (MPa)	EM (GPa)
5A06	2.64	117	24.7×10 ⁻⁶	325	160	68
Ti6Al4V	4.44	7.95	8.6 ×10 ⁻⁶	967	860	112

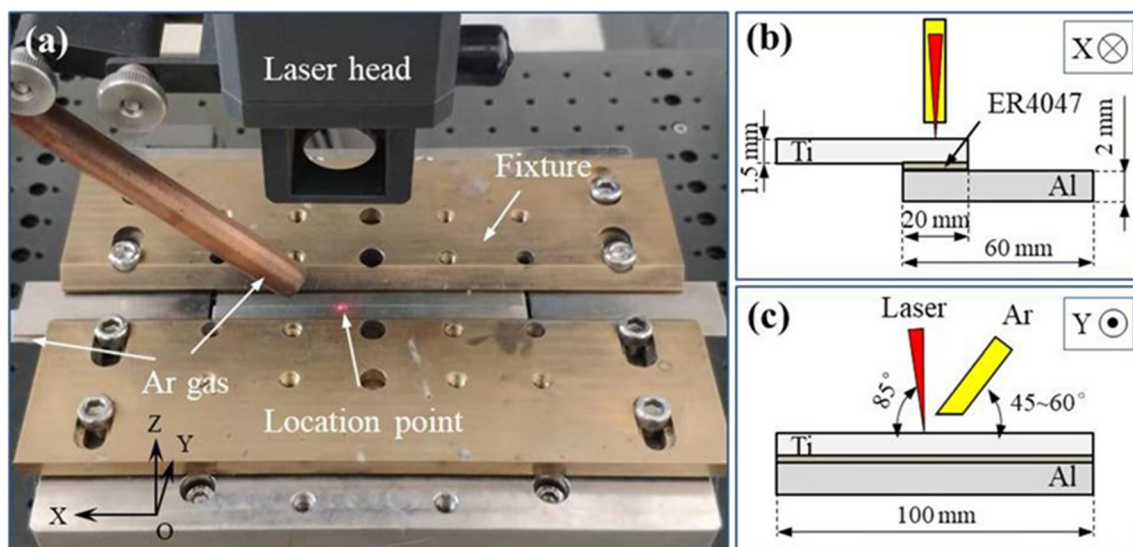
Table 3 The welding parameters

Sample number	#1 direct joint	#2 ER4047-added joints	#3	#4
ER4047 thickness, mm	0	0.1	0.2	0.3
Laser power, kW	1.2			
Defocusing distance, mm	0			
Welding speed (V), mm/s	14			
Overlap distance, mm	20			
Shielding gas flow rate, (L/min)	Front	20		
	Back	10		

According to Fig. 4 b and c, it is observed that both the weld depth (D) and penetration depth (P) decrease with the ER4047 thickness. It can be explained that when the laser beam penetrates into the ER4047 interlayer from the Ti6Al4V plate, part of the laser heat is lost between the layers, resulting in the sharp decrease of the penetration depth of the 5A06 plate [29]. Therefore, the thicker the ER4047 interlayer, the greater the heat loss and the smaller the whole depth of laser penetration. As presented in Fig. 4b, when the ER4047 thickness increases to 0.1 mm, the heating width of the molten pool decreases owing to the heat loss at ER4047 interlayer, resulting in the decline of the W_w . When the ER4047 thickness is greater than 0.1 mm, the W_w increases from 2267 to 2585 μm , which can be explained that the decrease of D makes the molten pool expand laterally. As shown in Fig. 4c, with the ER4047 thickness increases to 0.2 mm, the W_c increases from 617 to 700 μm because of the lower melting point of ER4047. However, when the ER4047 thickness is 0.3 mm, the transverse heating width begins to decrease as a result of the significant increasing of the heat loss at ER4047 interlayer, leading to the decrease of W_c .

Figure 4d shows the variation of weld depth to width ratio (R_w) and penetration depth to width ratio (R_p) against ER4047 thickness. The R_w decreases with the ER4047 interlayer thickness, indicating that the whole weld seam becomes more short and fat with the ER4047 interlayer thickness, as shown in the upper part of Fig. 4d. In addition, the R_p decreases straight first and then increases slowly, suggesting that the pudgy degree of the penetration layer increases first and then decreases. As shown in the lower left of Fig. 4d, the penetration layer of weld seam #3 is the shortest and fattest, and the remaining weld seams are #4, #2, and #1 in descending order from high to low.

Figure 5 shows the cross section morphology of the joints with different thickness of ER4047 interlayer. According to the weld seam surface profile marked in the upper right corner of the picture, when ER4047 interlayer is not added, the middle part of the weld protrudes upward, but a slight undercut occurs in the weld seam. When the ER4047 interlayer is added, the middle part is almost flat with the surface of the upper sheet, and the undercut of

**Fig. 1** a Physical drawing of laser welding process; b schematic diagram of X direction; c schematic diagram of Y direction

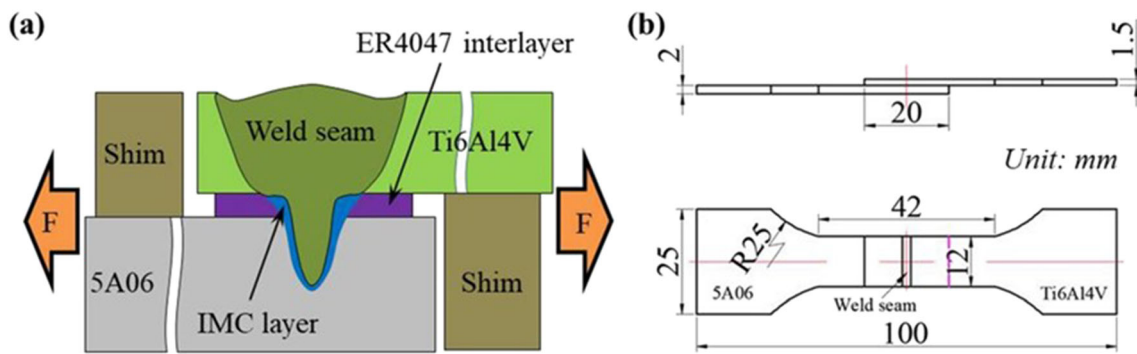


Fig. 2 The setup of the shear test: **a** loading schematic; **b** dimension of the shear test sample

weld seam increases with the ER4047 thickness. This can be explained that the increasing spatters originated from the ER4047 interlayer (Fig. 3) could cause serious loss of molten metal in molten pool, which leads to the increase of undercut [24, 29]. Furthermore, as shown in Fig. 5a, a small number of large pores appear at the weld bottom of direct joint, which can be explained that bubbles are difficult to escape upward and deposit in the bottom of weld to form large pores under the effect of the sharp fluctuation of keyhole shape [30, 31]. However, when the ER4047

interlayer is added, the vaporization of low melting point alloying elements intensifies, and the hydrogen is easily decomposed and penetrates into the molten pool, resulting in the appearing of the small and dense pores at the bottom of the weld, as shown in Fig. 5b–d [32, 33]. Moreover, as shown in Fig. 4a, a small number of holes also appear in the HAZ 2. These holes may be pores, originated from bubbles floating at the bottom of the molten pool or infiltrating from the air, or may be molten holes formed by over-melting of ER4047 layer [31, 34].

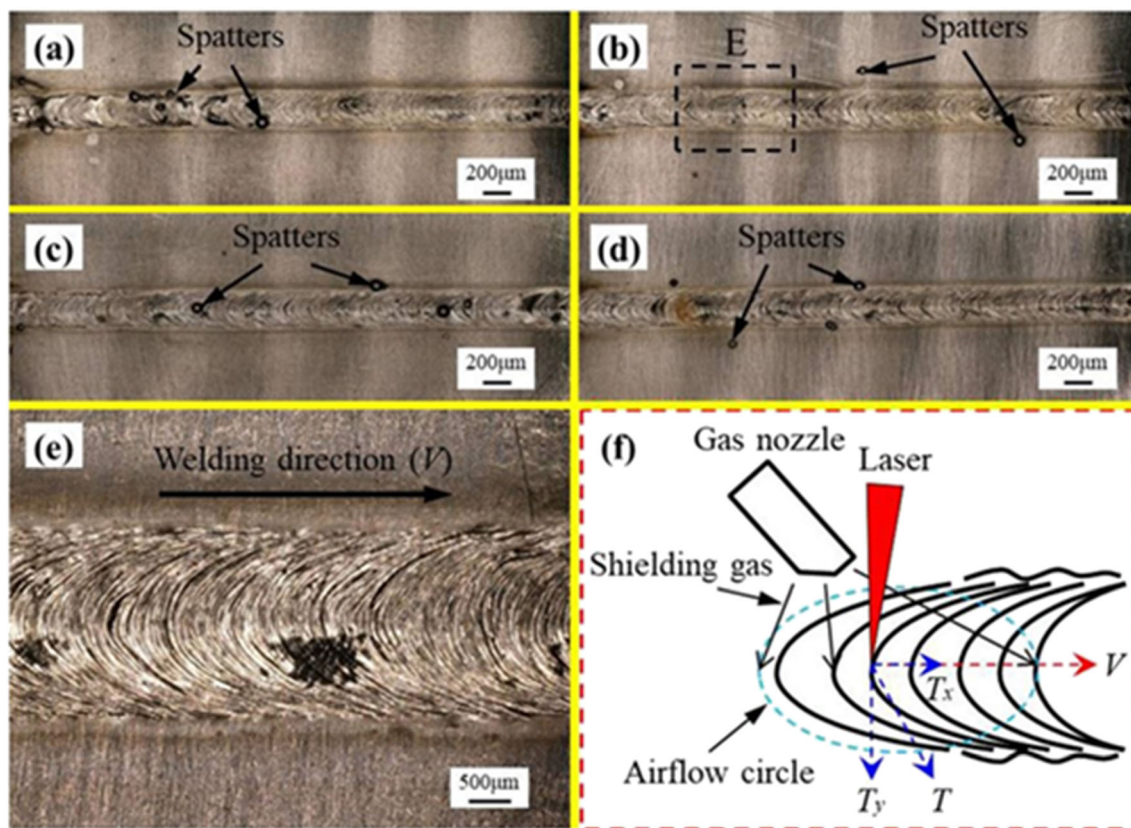


Fig. 3 Top surface appearance of welded joints with ER4047 interlayer thickness of **a** 0 mm, **b** 0.1 mm, **c** 0.2 mm, and **d** 0.3 mm; **e** magnification of area E marked in Fig. 3b; **f** schematic diagram of wave pattern formation

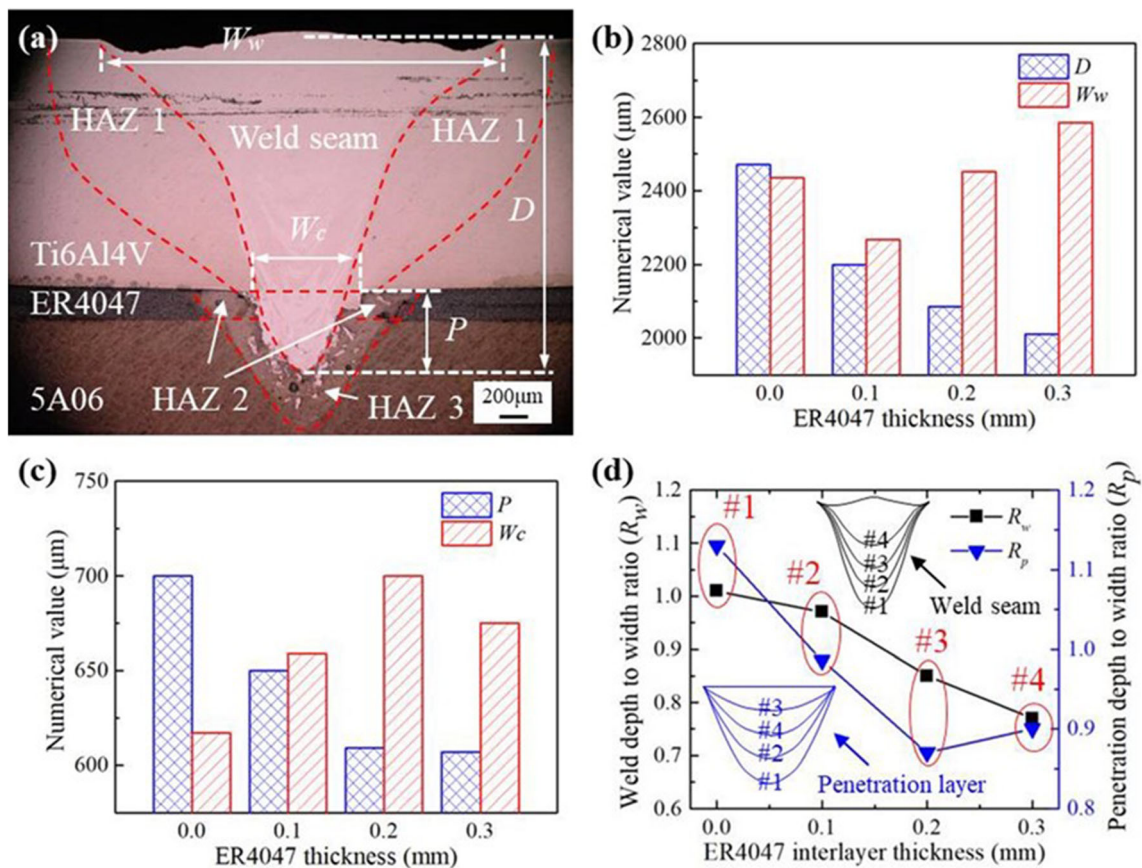


Fig. 4 Macroscopic cross section of the Ti/Al dissimilar lap joint: **a** cross section characteristics of the typical joint; **b** the variation of weld depth (D) and weld width (W_w) against ER4047 thickness; **c** the variation of penetration depth (P) and weld width at the upper coincidence surface

(W_c) against ER4047 thickness; **d** the variation of weld depth to width ratio (R_w) and penetration depth to width ratio (R_p) against ER4047 thickness

3.2 Elements distribution and interface layer analysis

3.2.1 Element distribution

The distribution of major alloying elements on cross section of the direct joints and ER4047-added joints shown in Fig. 6 depicts the diffusion and migration of the atoms. As shown in Fig. 6c, obvious melt holes are formed in ER4047 interlayer under the effect of higher heat transfer from 5A06 plate. According to the distribution of Al and Ti atoms of both direct joints and ER4047-added joints, it can be noted that under the action of metal vapor pressure, self-gravity, and recoil pressure, the fusion of upper and lower metal liquids results in the distribution of a large amount of Ti atoms and a small amount of Al atoms in the weld seam [35]. Moreover, the Ti atoms diffuse rapidly around the weld seam/Al interface [36]. Unlike Ti and Al atoms, the Si atoms in the direct joints are almost invisible because of low content in base metal, while the Si atoms in the ER4047-added joints enrich to the weld seam/Al interface. As shown in Fig. 6l, when the ER4047 interlayer thickness is 0.2 mm, the enrichment of Si atoms along the interface layer is the most obvious. It can be observed that

with the addition of ER4047 interlayer, the diffusion of Si atoms is strengthened, which effectively changes the composition of the weld seam [37, 38].

3.2.2 Prediction of IMCs formation

Because the generation of IMCs is closely related to the mechanical properties of the whole joint, it is of great significance to study the formation mechanism of Ti-Al IMCs. It is well known that the Gibbs free energy formation (ΔG) is an authoritative criterion for judging whether a chemical reaction occurs spontaneously. Specifically, when ΔG is greater than or equal to zero, the chemical reaction is in a state of non-spontaneous and equilibrium, respectively. Furthermore, when ΔG is less than zero, the chemical reaction can proceed spontaneously, and the smaller the ΔG value, the greater the possibility and trend of the chemical reaction. According to the Ti-Al phase diagram shown in Fig. 7a, it is noted that several IMCs, namely, $TiAl_3$, $TiAl$, $TiAl_2$, and Ti_3Al , may be formed in the Ti-Al system during the welding solidification process. To predict the formation order of the four IMCs near the Ti/Al interface, the effective way is to calculate the

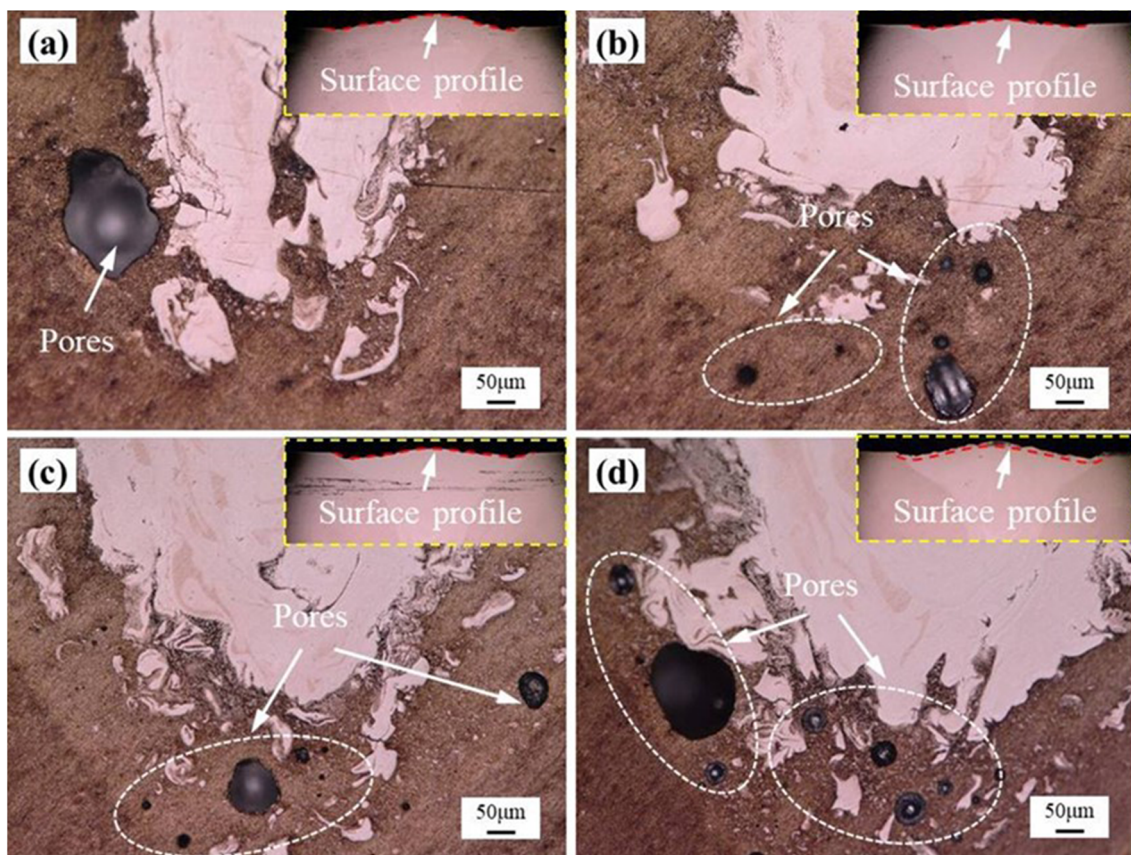


Fig. 5 OM images of weld seam cross section with ER4047 thickness of a 0 mm, b 0.1 mm, c 0.2 mm, and d 0.3 mm

ΔG of corresponding chemical reactions. According to the classical thermodynamic theory, the ΔG is represented by the first approximate equation as follows [39]:

$$\Delta G_T^\theta = \Delta H_{298}^\theta - T\Delta S_{298}^\theta \tag{1}$$

where θ represents the standard atmospheric pressure state ΔH_{298}^θ and ΔS_{298}^θ are standard enthalpy and entropy variations, respectively, and calculated according to the following formulas:

$$\Delta H_{298}^\theta = \sum \left(n_j \Delta H_{j,f,298}^\theta \right)_{(Products)} - \sum \left(n_i \Delta H_{i,f,298}^\theta \right)_{(Reactants)} \tag{2}$$

$$\Delta S_{298}^\theta = \sum \left(n_j S_{j,298}^\theta \right)_{(Products)} - \sum \left(n_i S_{i,298}^\theta \right)_{(Reactants)} \tag{3}$$

where $\Delta H_{i,f,298}^\theta$ and $\Delta H_{j,f,298}^\theta$ are the standard molar heat of formation of reactants and products and $S_{i,298}^\theta$ and $S_{j,298}^\theta$ are the standard molar entropy of reactants and products, respectively. The n_i and n_j are the quantities of reactants and products, respectively. By using the thermodynamic database of Ti-Al binary system in references [40–42] and substituting into Eqs. (1) to (3), the calculated Gibbs energy functions of Ti-Al IMCs can be obtained as follows:

$$\Delta G_{TiAl_3}^\theta = -142256 + 21.032T \tag{4}$$

$$\Delta G_{TiAl}^\theta = -72802 + 6.648T \tag{5}$$

$$\Delta G_{Ti_3Al}^\theta = -32251 + 6.986T \tag{6}$$

Based on the above equations, the relationship between ΔG and the temperature (at the range of 0–1200 °C) is shown in Fig. 7b. According to the calculated results of ΔG , it can be concluded that the metallurgical reaction of $TiAl_3$ is likely to happen first compared with Ti_3Al and $TiAl$ because of the lowest Gibbs free energy of formation, $TiAl$ is the second, and Ti_3Al is the last.

Figure 7c and d show the formation process of the molten pool. As displayed in Fig. 7c, when the laser beam radiates on the Ti6Al4V plate, the upper Ti6Al4V titanium alloy melts and evaporates quickly to form the sagging molten pool under the force of high temperature metal vapor and plasma [43]. As the laser beam moves, the molten pool reaches its maximum depth, and the molten metal no longer flows downward. During the subsequent process, the molten metal flows upward and outward from the bottom of the molten pool to the border of molten pool under the action of the buoyancy, back-flow of molten metal, and surface tension [44, 45], as

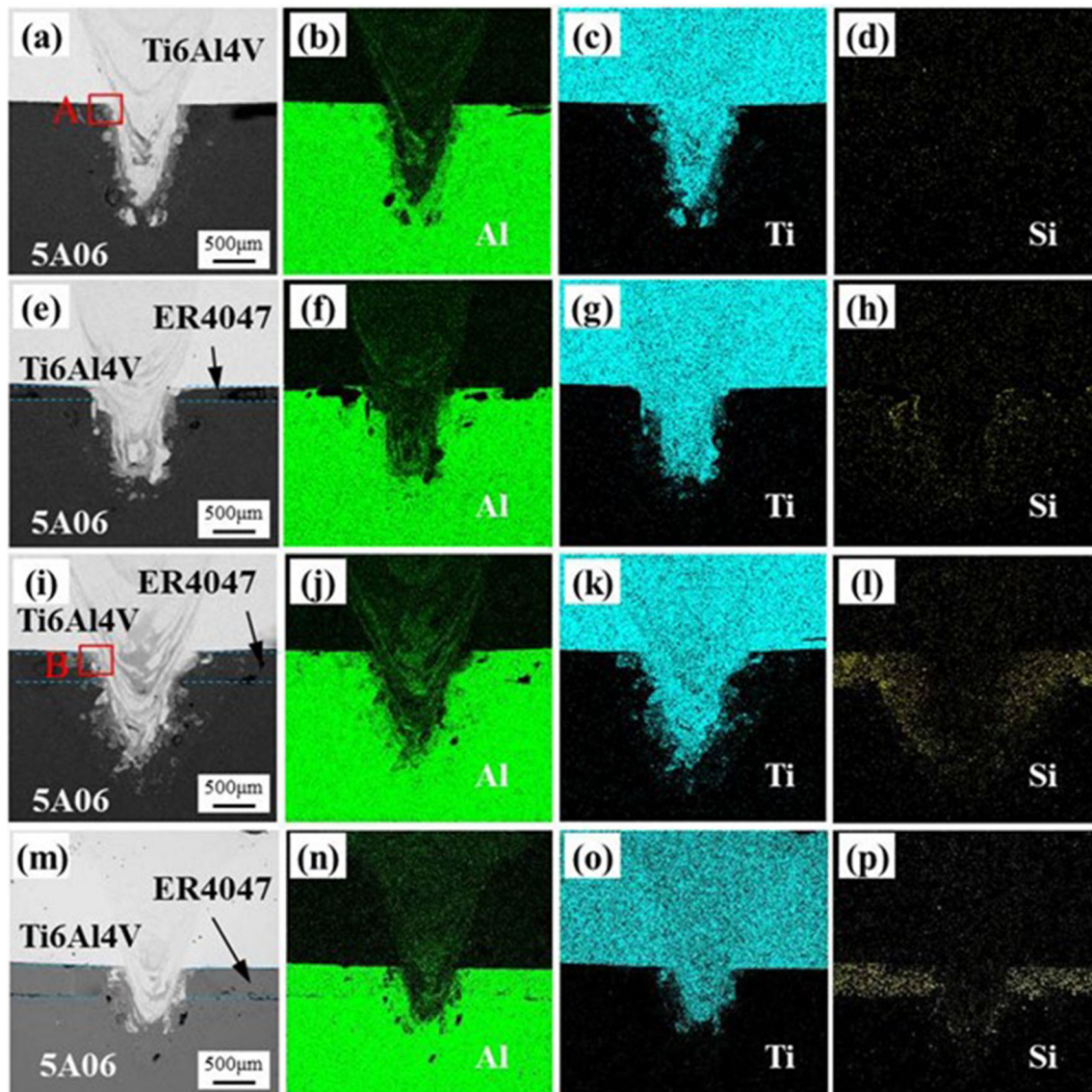


Fig. 6 Mapping analysis results of the joints with ER4047 interlayer thickness of **a–d** 0 mm, **e–h** 0.1 mm, **i–l** 0.2 mm, and **m–p** 0.3 mm

illustrated in Fig. 7d. Meanwhile, the IMC layers are beginning to form gradually at the molten pool/Al interface. Figure 7e–h show the formation stages of IMCs. Compared with the solubility of Al atom in titanium, the solubility of titanium in aluminum is extremely limited, indicating that the formation of IMCs is closely related to the diffusion of aluminum [46]. As shown in Fig. 7e, Ti atoms begin to diffuse to the outside of molten pool, while a large number of Al atoms begin to diffuse to the inner direction of molten pool. A small amount of Si atoms also migrate slowly to the molten pool/Al interface. Under the action of flowing liquid-mixed metal, a small amount of molten Ti is brought into the Al fusion zone to form some small liquid masses. Because of the presence of α -Ti stable elements, phase transformation α -Ti \rightarrow β -Ti is suppressed, and a thin α -Ti is formed in the molten pool near the molten pool/Al interface [30].

According to the reaction temperature and ΔG of different IMCs shown in Fig. 7a and b, it can be found that the reactions $\text{Ti} + 3\text{Al} \rightarrow \text{TiAl}_3$, $\text{Ti} + \text{Al} \rightarrow \text{TiAl}$, and $3\text{Ti} + \text{Al} \rightarrow \text{Ti}_3\text{Al}$ may take place from the Al-rich side to Ti-rich side [47], and the TiAl_3 , TiAl , and Ti_3Al layers will be formed orderly from outside to inside at the molten pool/Al interface, as displayed in Fig. 7f and g. Meanwhile, the dispersed titanium liquid masses begin to solidify, and separated TiAl_3 masses are formed near the Al fusion zone. Most importantly, the formation of IMCs, especially the growth of the serrated TiAl_3 layer, has blocked the diffusion channels of atoms inside and outside the molten pool very difficult. As the higher concentration of Al in the molten pool center, the transformation β -Ti \rightarrow α -Ti + Ti_3Al takes place during the rapid solidification process of molten pool [48, 49], and the Ti_3Al is formed adjacent to α -Ti layer.

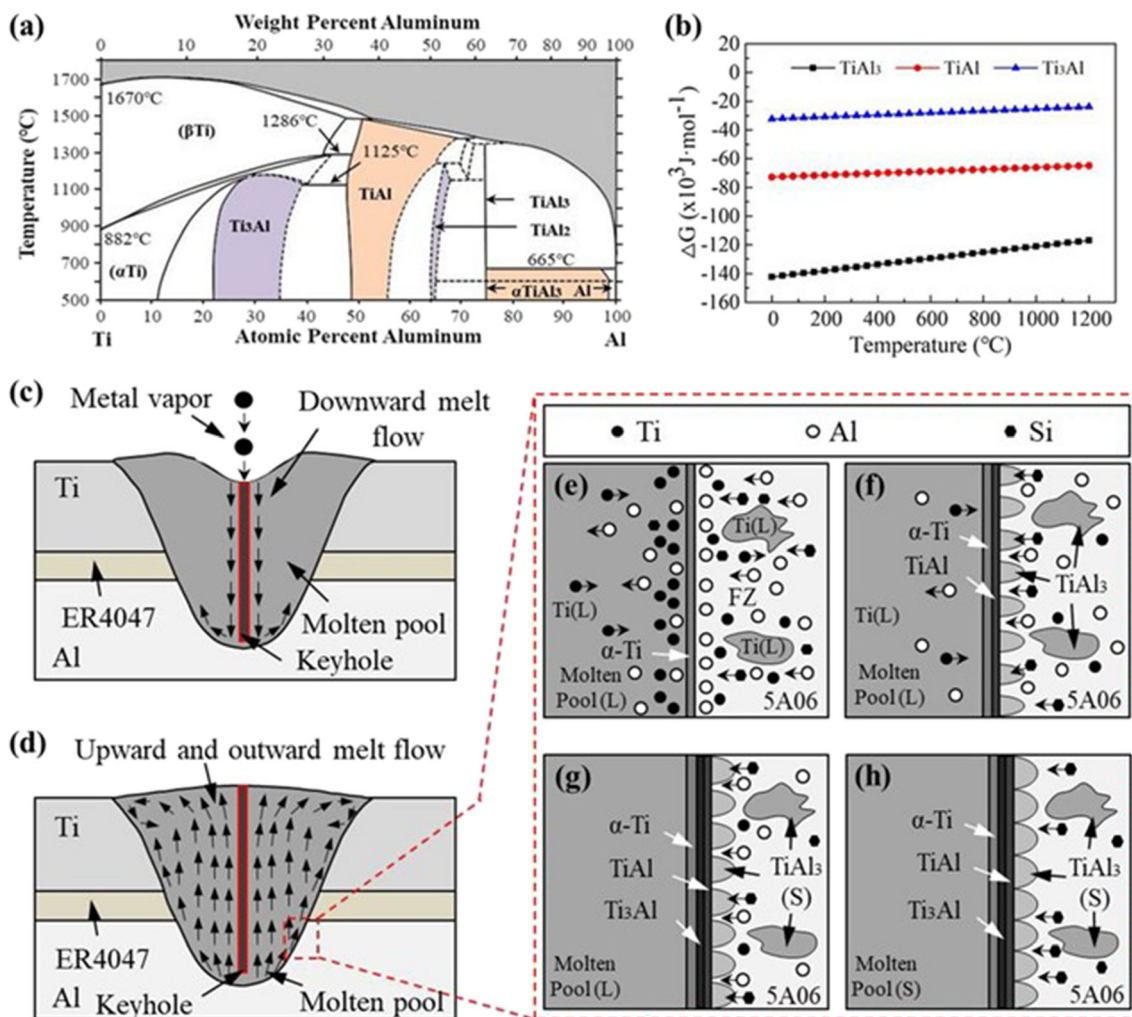


Fig. 7 **a** Ti-Al phase diagram; **b** Gibbs free energy (ΔG) of the formation of Ti-Al IMCs at various temperatures; **c** initial stage of melt flow in molten pool; **d** stable stage of melt flow in molten pool; **e–h** formation stages of IMCs at the molten pool/Al interface

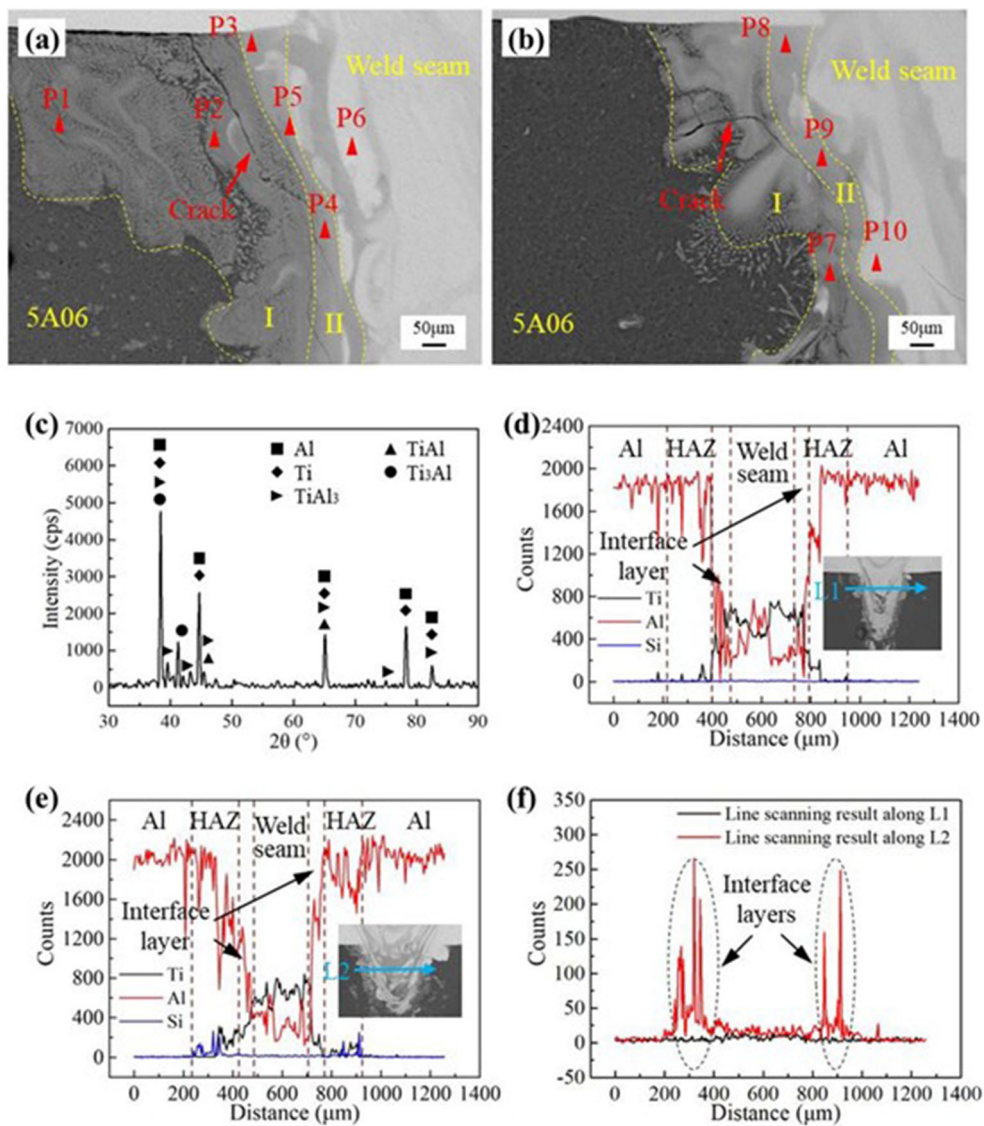
As shown in Fig. 7h, the Si atoms diffuse continuously from the Al fusion zone to the reaction layers at the final stage because of the lower potential energy of Si in solid Ti-Al IMCs, which can be demonstrated in Fig. 6l. It can be

observed from Fig. 7h that the sequence of the final IMCs at the molten pool/Al interface is $TiAl_3$, $TiAl$, and Ti_3Al in turn from outside to inside, and the conclusion needs to be further proved by subsequent experiments.

Table 4 EDS point scanning results marked in Fig. 8

Testing point	Ti (at.%)	Al (at.%)	V (at.%)	Mg (at.%)	Si (at.%)	Possible Ti-Al phases
P1	20.16	78.06	0.73	0.96	0.09	$TiAl_3$
P2	23.33	75.25	0.97	0.37	0.07	$TiAl_3$
P3	43.66	54.44	1.48	0.36	0.06	$TiAl$
P4	38.00	59.31	1.42	1.21	0.05	$TiAl$
P5	66.84	30.45	2.25	0.20	0.27	Ti_3Al
P6	75.77	21.49	2.42	0.22	0.11	Ti_3Al
P7	29.88	66.00	1.07	1.25	1.79	$TiAl_3$
P8	49.37	46.61	1.49	0.17	2.36	$TiAl$
P9	43.60	51.74	1.45	0.18	3.02	$TiAl$
P10	76.32	20.32	2.54	0.11	0.71	Ti_3Al

Fig. 8 **a** SEM magnified image of area A in Fig. 6a; **b** SEM magnified image of area B in Fig. 6i; **c** XRD results at weld seam/Al interface of the typical joint; **d** EDS line scanning result of direct joints along L1; **e** EDS line scanning result of the ER4047-added joints with the thickness of 0.2 mm along L2; **f** EDS line scanning results of Si element along L1 and L2, respectively

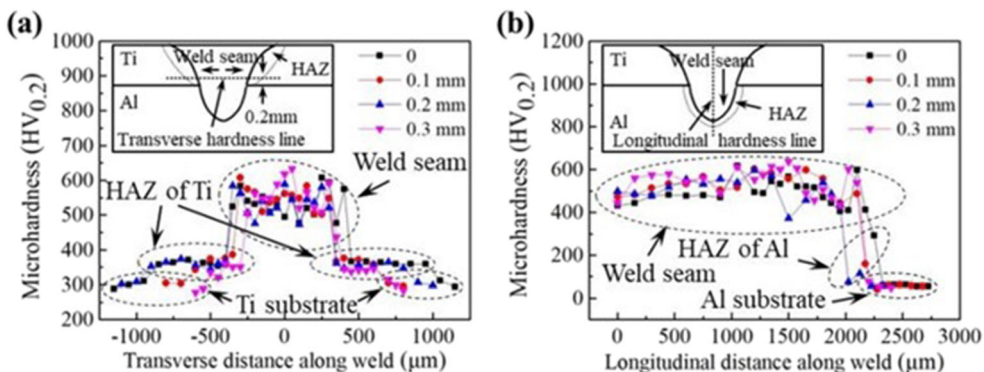


3.2.3 Experimental verification of interface layer

The weld interface of the joints was subjected to SEM and XRD observations in order to investigate the composition phase of the IMCs at the weld seam/Al interface. Figure 8a

and b show the SEM images of the weld seam/Al interface of the direct and ER4047-added joints, and the results of EDS scanning and XRD scanning are shown in Table 4 and Fig. 8c, respectively. It can be seen that the IMCs layers of both direct joints and ER4047-added joints mainly consist of three layers,

Fig. 9 Micro-hardness of the joints with different ER4047 interlayer thickness along different testing lines: **a** transverse hardness line at Ti side; **b** longitudinal hardness line at the weld seam center



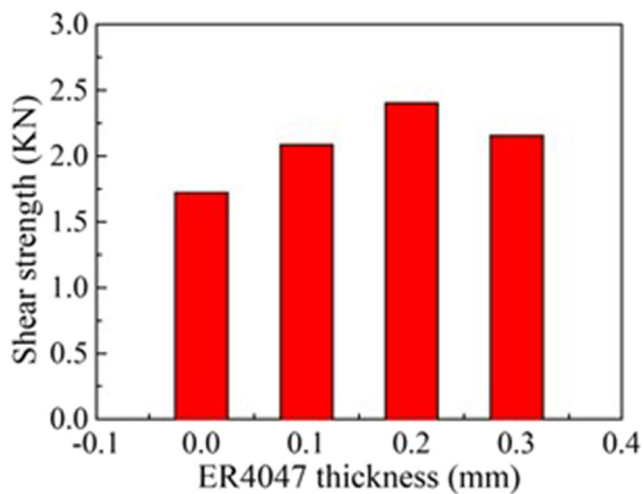
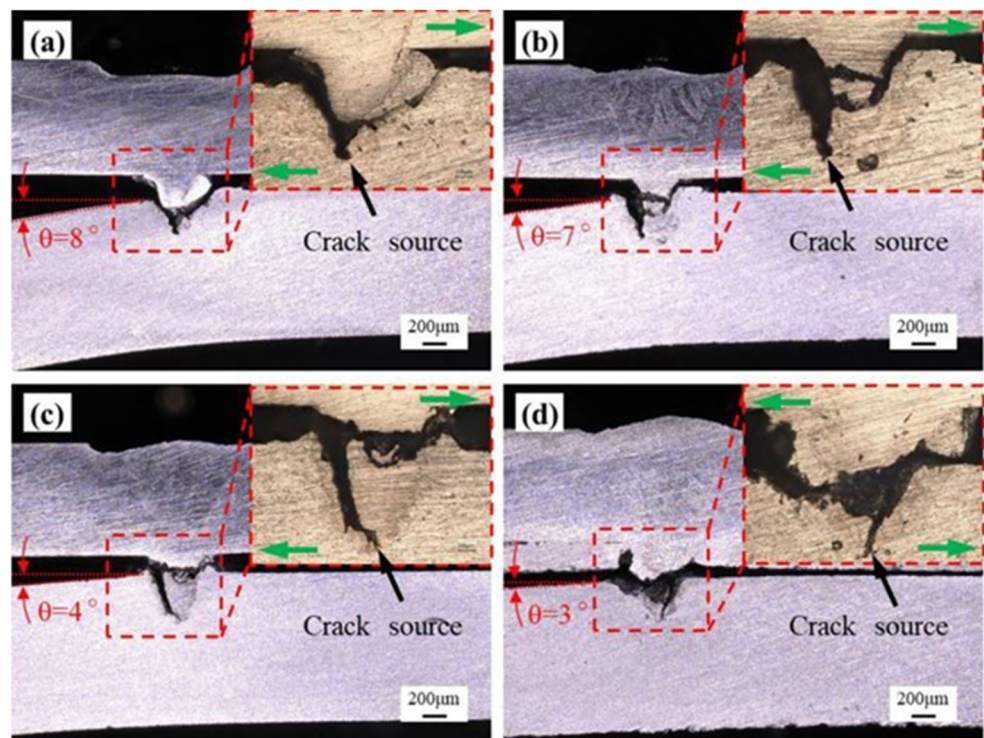


Fig. 10 The shear strength of the joints against ER4047 interlayer thickness

namely, the outmost TiAl_3 layer (marked as I), the middle TiAl layer (marked as II), and the inmost Ti_3Al layer [50], which is consistent with the results discussed in Section 3.2.2. According to Fig. 8a and b, the TiAl_3 layer is far thicker than TiAl layer due to the faster growth rate during the solidification process. Moreover, the TiAl_3 thickness of the ER4047-added joints is obviously thinner than that of the direct joints, indicating that the addition of ER4047 can inhibit the growth of the IMCs, which has been confirmed by Shuhai Chen [25]. However, under larger thermal stress, the Ti_3Al layer is also prone to cracks, and failure usually occurs in this layer. It is worth noting that the existence of Si atoms at

Fig. 11 Fracture locations of the joints with ER4047 interlayer thicknesses of a 0 mm, b 0.1 mm, c 0.2 mm, and d 0.3 mm



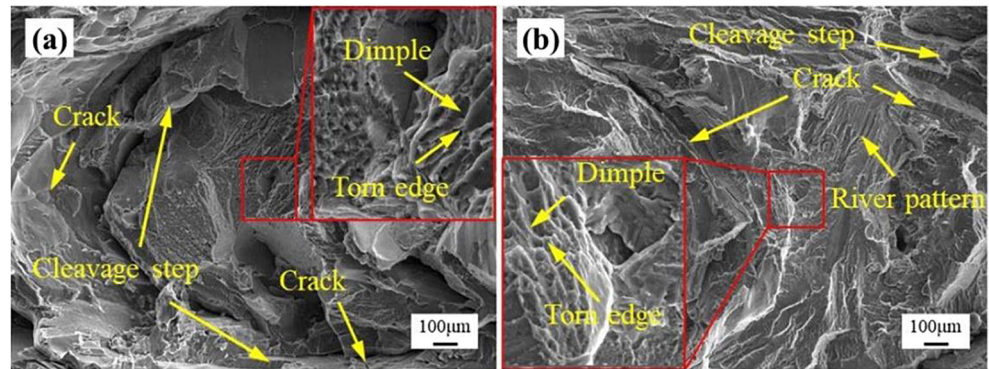
HAZ of Al originating from the ER4047 interlayer reduces the brittleness and cracking tendency of the joint to a certain extent [51, 52]. Figure 8d and e present the line scanning results of direct joint and ER4047-added joint, respectively. It can be observed that the distribution of Ti, Al, and Si atoms is not uniform, and the fluctuation is the greatest at the interface layer. As shown in Fig. 8f, with the addition of the intermediate layer, the Si atoms at the interface layer increase sharply (Fig. 6h, l, and p) to inhibit the formation of IMCs because of the lower potential energy [52, 53].

3.3 Mechanical property of the joint

3.3.1 Micro-hardness of the joint

Micro-hardness of joints without interlayer and with different thicknesses of ER4047 interlayers shown in Fig. 9 was measured across the weld cross section from transverse direction and longitudinal direction. According to Fig. 9a, the hardness at weld seam of both direct and ER4047-added joints fluctuated mainly between 470 and 600 HV and is higher than the other zones, which is mainly due to the formation of IMC mixed layers [54]. Moreover, the hardness of HAZ on Ti side is 340–360 HV, which is slightly higher than that of titanium base metal (305 HV). It can be explained that the β phase in HAZ transforms into needle-like martensite phase α' during the rapid solidification process [55], and the hardness at this zone is significantly improved due to the formation of the phase α' . As displayed in Fig. 9b, the hardness at weld seam

Fig. 12 Fracture surface of **a** the direct joint and **b** the ER4047-added joint



in longitudinal direction of both direct joints and ER4047-added joints varies from 400 to 600 HV because of the formation of IMC mixed layers. In addition, the hardness of HAZ on Al side is 100–200 HV, which is greater than that of aluminum base metal (50 HV) due to the diffusion of Ti atoms and effect of quenching.

3.3.2 Shear strength of the joint

Figure 10 shows the effect of ER4047 interlayer thickness on the shear strength of the joint. It is not difficult to find that the shear strength increases first and then decreases with the ER4047 interlayer thickness. The shear strength of direct joint is only 1721 N, while the shear strength of the ER4047-added joints is 2087 N, 2405 N, and 2157 N, respectively, which indicates that the 0.2 mm thick ER4047 interlayer is suitable for this experiment. The variation of penetration depth (P) with ER4047 interlayer thickness displayed in Fig. 4c can explain the shear strength value of different joints shown in Fig. 10. For the direct joints, the higher P usually induces thicker IMC layer at the weld seam/Al interface [56], and the macro-crack (Fig. 8a) is easily to form at the interface, leading to the fact that the joints are prone to fracture along the interface, as shown in Fig. 11a. Thus, the shear strength of direct joints is the lowest. After adding 0.1 mm and 0.2 mm thick ER4047 interlayer, the IMC layers decrease owing to the smaller P and the inhibition action of the silicon, resulting in the change of fracture mode. As depicted in Fig. 11b and c, the fracture position is shifted to the middle layer of the weld seam with higher strength, which significantly increases the shear strength of the joints. However, when the ER4047 interlayer thickness reaches 0.3 mm, the shear strength of the joints decreases again because of the excessively smaller P [57], resulting in the fact that the fracture occurs along the interface again, as displayed in Fig. 11d. Moreover, as shown in Fig. 11, the deformation decreases gradually with the increase of the thickness of ER4047 interlayer. When the ER4047 interlayer is added, the value of P decreases with the increase of ER4047 thickness (Fig. 4c), and the crack on the left side of the weld becomes shallow. As a result, the shear moment

around the bottom of the crack decreases gradually, which leads to the reduction of deformation.

3.4 Fracture surface

Figure 12 shows the local fracture morphology of the direct joint and the ER4047-added joint. According to Fig. 12a, the fracture surface of the direct joint exhibits the clear boundaries between rough areas and other areas, and the smooth surface with some higher cleavage steps and cracks is much larger than the rough surface with some dimples and torn edges shown in the magnified image. Therefore, the fracture surface of direct joint presents brittle characteristics on the whole and belongs to brittle fracture surface, resulting in the lower tensile strength of the joint. However, the fracture surface of the ER4047-added joint shown in Fig. 12b not only displays the cleavage fracture features such as river patterns and cleavage steps but also shows the plastic fracture features such as dimples and torn edges [58], implying that the fracture surface of ER4047-added joint is the quasi-cleavage fracture surface. So, the shear strength of the ER4047-added joint is much higher than that of direct joint.

4 Conclusions

Laser penetration of Ti6Al4V titanium alloy to 5A06 aluminum alloy without and with the addition of ER4047 interlayer has been studied. The formation of weld seam, microstructure, interfacial growth process, and mechanical properties of both direct joints and ER4047-added joints were investigated in detail. Based on the calculation results of free energy of IMCs formation, the formation process of IMCs at the interface was discussed, and the calculated results were in good agreement with the experimental results. The key results can be summarized as follows:

- (1) The spatters on the top surface of ER4047-added joints are more intensive than that of direct joints, which indicates that the addition of interlayer accelerates the

evaporation of low melting point alloy elements to a certain extent and causes the instability of molten pool.

- (2) According to the calculated results of Gibbs free energy and experimental results, the formation order of IMC layer at weld seam/Al interface of both direct joints and ER4047-added joints is $TiAl_3$, $TiAl$, and Ti_3Al , which indicating that the process of calculation and analysis is reasonable.
- (3) The results of micro-hardness tests along the transverse hardness line at the Ti side of both direct joints and ER4047-added joints show that the hardness of the weld seam is the highest, followed by the HAZ and the titanium base metal, which is attributed to the formation of IMC mixed layer at the weld seam and the needle-like martensite at the HAZ. Moreover, the Ti atoms diffuse into the HAZ of aluminum, which makes the room temperature hardness of this zone significantly higher than that of aluminum base metal.
- (4) The shear strength of ER4047-added joints is generally higher than that of direct joints, and the maximum shear strength of ER4047-added joints can reach 2405 N with the 0.2 mm thick interlayer, and the shear strength of direct joints is only 1721 N. Moreover, the fracture type of the direct joint is brittle fracture, while that of the ER4047-added joints is quasi-cleavage, indicating that the addition of ER4047 interlayer improves the brittleness of joints to a certain extent.

Author contributions Fan Zhang and Ji'an Duan proposed this work and gave guidance to the writing and revision of the manuscript; Xiongfeng Zhou and Xiaobing Cao performed the experiments; Xiongfeng Zhou and Zhi Chen analyzed the experiment data; Xiongfeng Zhou wrote the manuscript.

Funding This work was supported by the National Key Research and Development Program of China (Grant No. 2017YFB1104801).

References

1. Leo P, D'Ostuni S, Casalino G (2018) Low temperature heat treatments of AA5754-Ti6Al4V dissimilar laser welds: microstructure evolution and mechanical properties. *Opt Laser Technol* 100:109–118
2. Auwal ST, Ramesh S, Yusof F, Manladan SM (2018) A review on laser beam welding of titanium alloys. *Int J Adv Manuf Technol* 97:1071–1098
3. Zhang Y, Huang JH, Ye Z, Cheng Z (2017) An investigation on butt joints of Ti6Al4V and 5A06 using MIG/TIG double-side arc welding-brazing. *J Manuf Process* 27:221–225
4. Shi JM, Feng JC, Liu H, Tian XY, Zhang LX (2017) Vacuum brazing of the Gr/2024Al composite and TC4 alloy using AgCuTi filler alloy with Ni-Al interlayer as auxiliary heat source. *J Alloys Compd* 694:672–681
5. Zhou L, Yu M, Jiang Z, Guo F, Zhao H, Huang Y, Song X (2019) Influence of rotation speed on microstructure and mechanical properties of friction stir lap welded joints of AA 6061 and Ti6Al4V alloys. *Metall Mater Trans A* 50:733–745
6. Kuryntsev SV (2019) Microstructure, mechanical and electrical properties of laser-welded overlap joint of CP Ti and AA2024. *Opt Lasers Eng* 112:77–86
7. Möller F, Thomy C, Vollertsen F (2012) Joining of titanium-aluminium seat tracks for aircraft applications system technology and joint properties. *Weld World* 56:108–114
8. Vaidya WV, Horstmann M, Ventzke V, Petrovski B, Kocak M, Kocik R (2010) Tempus, improving interfacial properties of a laser beam welded dissimilar joint of aluminium AA6056 and titanium Ti6Al4V for aeronautical applications. *J Mater Sci* 45:6242–6254
9. Zhang YF, Huang J, Ye Z, Cheng Z, Yang J, Chen SH (2018) Influence of welding parameters on the IMCs and the mechanical properties of Ti/Al butt joints welded by MIG/TIG double-sided arc welding-brazing. *J Alloys Compd* 747:764–771
10. Plaine AH, Gonzalez AR, Suhuddin UF, dos Santos JF, Alcantara NG (2016) Process parameter optimization in friction spot welding of AA5754 and Ti6Al4V dissimilar joints using response surface methodology. *Int J Adv Manuf Technol* 85:1575–1583
11. Casalino G, Mortello M (2016) Modeling and experimental analysis of fiber laser offset welding of Al-Ti butt joints. *Int J Adv Manuf Technol* 83:89–98
12. Vacchi GS, Plaine AH, Silva R, Sordi VL, Suhuddin UFH, Alcantara NG, Kuri SE, Rovere CAD (2017) Effect of friction spot welding (FSpW) on the surface corrosion behavior of overlapping AA6181/Ti-6Al-4V joints. *Mater Des* 131:127–134
13. Fang Y, Jiang X, Mo D, Zhu D, Luo Z (2019) A review on dissimilar metals' welding methods and mechanisms with interlayer. *Int J Adv Manuf Technol* 10:1–19
14. Kar A, Choudhury SK, Suwas S, Kailas SV (2018) Effect of niobium interlayer in dissimilar friction stir welding of aluminum to titanium. *Mater Charact* 145:402–412
15. Alhazaa AN, Khan TI (2010) Diffusion bonding of Al7075 to Ti-6Al-4V using Cu coatings and Sn-3.6Ag-1Cu interlayers. *J Alloys Compd* 494:351–358
16. Samavatian M, Khodabandeh A, Halvae A, Amadeh AA (2015) Transient liquid phase bonding of Al 2024 to Ti6Al4V alloy using Cu-Zn interlayer. *Trans Nonferrous Metal Soc* 25:770–775
17. Wang H, Yuan X, Li T, Wu K, Sun Y, Xu C (2018) TIG welding-brazing of Ti6Al4V and Al5052 in overlap configuration with assistance of zinc foil. *J Mater Process Technol* 251:26–36
18. Mohammadpour M, Yazdian N, Yang G, Wang HP, Carlson B, Kovacevic R (2018) Effect of dual laser beam on dissimilar welding-brazing of aluminum to galvanized steel. *Opt Laser Technol* 98:214–228
19. Taban E, Gould JE, Lippold JC (2010) Characterization of 6061-T6 aluminum alloy to AISI, steel interfaces during joining and thermo-mechanical conditioning. *Mater Sci Eng A* 527:1704–1708
20. Wang ZM, Oliveira JP, Zeng Z, Bu XZ, Peng B, Shao XY (2019) Laser beam oscillating welding of 5A06 aluminum alloys: microstructure, porosity and mechanical properties. *Opt Laser Technol* 111:58–65
21. Zhang Y, Sun DQ, Gu XY, Li HM (2018) Strength improvement and interface characteristic of direct laser welded Ti alloy/stainless steel joint. *Mater Lett* 231:31–34
22. Hao XH, Dong HG, Li S, Xu XX, Li P (2018) Lap joining of TC4 titanium alloy to 304 stainless steel with fillet weld by GTAW using copper-based filler wire. *J Mater Process Technol* 257:88–100
23. Zhou XF, Duan JA, Zhang F, Zhong SS (2019) The study on mechanical strength of titanium-aluminum dissimilar butt joints by laser welding-brazing process. *Mater* 12:712
24. Li SC, Chen GY, Katayama S, Zhang Y (2013) Relationship between spatter formation and dynamic molten pool during high-power deep-penetration laser welding. *Appl Surf Sci* 303:481–488

25. Chen SH, Yang DW, Li M, Zhang YH, Huang JH, Yang J, Zhao XK (2016) Laser penetration welding of an overlap titanium-on-aluminum configuration. *Int J Adv Manuf Technol* 87:3069–3079
26. Li S, Chen G, Zhang M, Zhou Y, Zhang Y (2014) Dynamic key-hole profile during high-power deep-penetration laser welding. *J Mater Process Technol* 214:565–570
27. Cui CY, Cui XG, Ren XD, Liu TT, Hu JD, Wang YM (2013) Microstructure and microhardness of fiber laser butt welded joint of stainless steel plates. *Mater Des* 49:761–765
28. Zhang MJ, Chen GY, Zhou Y (2013) Observation of spatter formation mechanisms in high-power fiber laser welding of thick plate. *Appl Surf Sci* 280:868–875
29. Ai YW, Jiang P, Wang CM, Mi GY, Geng SN (2018) Experimental and numerical analysis of molten pool and keyhole profile during high-power deep-penetration laser welding. *Int J Heat Mass Transf* 126:779–789
30. Lee SJ, Makoto T, Yousuke K, Seiji K (2015) Microstructural evolution and characteristics of weld fusion zone in high speed dissimilar welding of Ti and Al. *Int J Precis Eng Manuf* 16:2121–2127
31. Sun JH, Nie PL, Feng K, Li ZG, Guo BC, Jiang E (2017) The elimination of pores in laser welds of AISI 304 plate using different shielding gases. *J Mater Process Technol* 248:56–63
32. Zhang XH, Zhao YQ, Liu ZM, Gao QY, Bu HC (2018) Microstructure and porosity characteristics of 5A06 aluminum alloy joints using laser-MIG hybrid welding. *J Manuf Process* 35:437–445
33. Narsimhachary D, Dutta K, Shariff SM, Padmanabham G, Basu A (2019) Mechanical and microstructural characterization of laser weld-brazed AA6082-galvanized steel joint. *J Mater Process Technol* 263:21–32
34. Wang XJ, Meng QC, Hu WP (2020) Continuum damage mechanics-based model for the fatigue analysis of welded joints considering the effects of size and position of inner pores. *Int J Fatigue* 139:105749
35. Akbari M, Saedodin S, Panjehpour A, Hassania M, Afranda M, Torkamany MJ (2016) Numerical simulation and designing artificial neural network for estimating melt pool geometry and temperature distribution in laser welding of Ti6Al4V alloy. *Optik* 127:11161–11172
36. Choi JW, Liu HH, Fujii H (2018) Dissimilar friction stir welding of pure Ti and pure Al. *Mater Sci Eng A* 730:168–176
37. Ma JJ, Harooni M, Carlson B, Kovacevic R (2014) Dissimilar joining of galvanized high-strength steel to aluminum alloy in a zero-gap lap joint configuration by two-pass laser welding. *Mater Des* 58:390–401
38. Zhang ZQ, Tan CW, Zhao XY, Chen B, Song XG, Zhao HY (2018) Influence of Cu coating thickness on interfacial reactions in laser welding-brazing of Mg to Ti. *J Mater Process Technol* 261:61–73
39. Mei SW, Gao M, Yan J, Zhang C, Li G, Zeng XY (2013) Interface properties and thermodynamic analysis of laser-arc hybrid welded Al/steel joint. *Sci Technol Weld Join* 18:293–300
40. Peng LM, Wang JH, Li H, Zhao JH, He LH (2005) Synthesis and microstructural characterization of Ti-Al₃Ti metal-intermetallic laminate (MIL) composites. *Scr Mater* 52:243–248
41. Ohnuma I, Fujita Y, Mitsui H (2000) Phase equilibria in the Ti–Al binary system. *Acta Mater* 48:3113–3123
42. Schuster JC, Palm M (2006) Reassessment of the binary aluminum-titanium phase diagram. *J Phase Equilib Diffus* 27:255–277
43. Gao M, Chen C, Gu YZ, Zeng XY (2014) Microstructure and tensile behavior of laser arc hybrid welded Dissimilar Al and Ti alloys. *Mater* 7:1590–1602
44. Gao ZM, Jiang P, Mi GY, Cao LC, Liu W (2018) Investigation on the weld bead profile transformation with the keyhole and molten pool dynamic behavior simulation in high power laser welding. *Int J Heat Mass Transf* 116:1304–1313
45. Cho WI, Na SJ, Thomy C, Vollertsen F (2012) Numerical simulation of molten pool dynamics in high power disk laser welding. *J Mater Process Technol* 212:262–275
46. Li HX, Nie XY, He ZB (2017) Interfacial microstructure and mechanical properties of Ti6Al4V/Al7050 joints fabricated using the insert molding method. *Int J Miner Metall Mater* 24:1412–1423
47. Sun QJ, Li JZ, Liu YB, Li BP, Xu PW, Feng JC (2017) Microstructural characterization and mechanical properties of Al/Ti joint welded by CMT method-assisted hybrid magnetic field. *Mater Des* 116:316–324
48. Wang T, Li XP, Zhang YY, Li HJ, Zhang BG (2017) Regulating the interfacial morphology of electron beam welded pure Ti/2024Al dissimilar joint. *J Mater Process Technol* 245:227–231
49. Wei SZ, Li YJ, Wang J, Liu K (2014) Improving of interfacial microstructure of Ti/Al joint during GTA welding by adopting pulsed current. *Int J Adv Manuf Technol* 73:1307–1312
50. Kattner UR, Lin JC, Chang YA (1992) Thermodynamic assessment and calculation of the Ti–Al system. *Metall Mater Trans A* 23:2081–2090
51. Fang YJ, Jiang XS, Mo DF, Zhu DG, Luo ZP (2019) A review on dissimilar metals' welding methods and mechanisms with interlayer. *Int J Adv Manuf Technol* 13:13–21
52. Chen SH, Li LQ, Chen YB, Huang JH (2011) Joining mechanism of Ti/Al dissimilar alloys during laser welding-brazing process. *J Alloys Compd* 509:891–898
53. Gupta SP (2012) Intermetallic compounds in diffusion couples of Ti with an Al–Si eutectic alloy. *Mater Charact* 49:321–330
54. Song ZH, Nakata K, Wu AP, Liao JS (2013) Interfacial microstructure and mechanical property of Ti6Al4V/A6061 dissimilar joint by direct laser brazing without filler metal and groove. *Mater Sci Eng A* 560:111–120
55. Hong KM, Shin YC (2016) Analysis of microstructure and mechanical properties change in laser welding of Ti6Al4V with a multiphysics prediction model. *J Mater Process Technol* 237:420–429
56. Sierra G, Peyre P, Deschaux-Beaume F, Stuart D, Fras G (2007) Steel to aluminium key-hole laser welding. *Mater Sci Eng A Struct Mater Prop Microstruct Process* 447:197–208
57. Qi XD, Liu LM (2012) Fusion welding of Fe-added lap joints between AZ31B magnesium alloy and 6061 aluminum alloy by hybrid laser-tungsten inert gas welding technique. *Mater Des* 33:436–443
58. Tomashchuk I, Sallamand P, Cicala E, Peyre P, Grevey D (2015) Direct keyhole laser welding of aluminum alloy AA5754 to titanium alloy Ti6Al4V. *J Mater Process Technol* 217:96–104

Publisher's note Springer Nature remains neutral with regard to jurisdictional claims in published maps and institutional affiliations.